The International Journal of Advanced Manufacturing Technology (2022) 123:2261–2278
https://doi.org/10.1007/s00170-022-10311-2

ORIGINAL ARTICLE

Strengthening of duplex stainless steel processed by equal channel angular pressing (ECAP)

Jairo Alberto Muñoz[1,2] · Mohan Chand[1] · Javier Walter Signorelli[2] · Jessica Calvo[1] · José María Cabrera[1,3]

Received: 2 August 2022 / Accepted: 11 October 2022 / Published online: 27 October 2022

Abstract
This manuscript presents the study of the microstructural evolution, plastic anisotropy, and mechanical behavior of a duplex stainless steel (DSS) processed by the equal channel angular pressing (ECAP) technique. The ECAP process produced shear bands affecting both phases, austenite and ferrite, which in turns act as preferential sites for the appearance of the new ultrafine grains. Microstructural observations indicated grain sizes smaller than 300 nm in both phases. However, marked differences in the grain boundary misorientations were observed. Most ferrite grain boundaries showed low misorientations (average misorientation of 30°). In contrast, the austenite grain boundaries were mainly dominated by high-angle grain boundaries (average misorientation of 39°). The ECAP processing allowed to reach a yield strength over 1.1 GPa after one ECAP pass. Dislocations formed walls in the ferrite, while they were distributed evenly in the austenite grains creating plastic gradients between the two phases. Through the visco-plastic self-consistent model, it was found that austenite and ferrite strain hardening at different rates, generating plastic instabilities at different strain magnitudes. In this way, it was shown that austenite is the phase that provides more hardening while ferrite provides ductility. Regarding the anisotropy of the steel, crystal plasticity simulations showed that during the first passes of ECAP, the Lankford coefficients increase notably due to the heterogeneous microstructure of sheared grains with a higher density of defects forming subgrains in ferrite than austenite. Moreover, the austenite was more responsible for the larger planar anisotropy ($\Delta r = 2.18$) values than ferrite ($\Delta r = 1.67$) after two ECAP passes.

Keywords Duplex steel · Severe plastic deformation · Equal channel angular pressing · Texture · Crystal plasticity

1 Introduction

The mechanical and microstructural characterization of metallic materials such as steel is vital for their correct application in different industries. Therefore, special attention has to be paid to the study of steels that involve plastic deformation processes in production lines since their mechanical response can change radically concerning the deformation-free state [1–3]. This phenomenon is owed to a mechanism of change in the grain dimensions (< 1 μm) due to pronounced defects increments, mainly when the deformation is carried out at temperatures below the recrystallization temperature [4]. Thus, depending on the magnitude and mode of deformation, different thermomechanical processes and types of microstructures can be obtained [5, 6]. It is well known that true plastic strains greater than 3 can be applied, for example, through traditional and widely known processes such as rolling, drawing, deep-drawing, forging, and extrusion obtaining grain structures of the micrometric order [7]. However, the aforementioned processes cause anisotropy because they involve monotonic deformations, generating elongated grains with a well-defined texture [8, 9]. There are alternative processes which provoke ultrafine grain materials (UFG) that stand out not only for their prominent mechanical properties but also for their physical properties. These processes allow to obtain microstructures in metallic materials with hybrid properties such as high mechanical strength together with good electrical conductivity, and/

✉ Jairo Alberto Muñoz
jairomunoz8614@gmail.com; jairo.alberto.munoz@upc.edu

[1] Department of Materials Science and Engineering EEBE, Universidad Politécnica de Catalunya, c/Eduard Maristany 10-14, 08019 Barcelona, Spain

[2] Instituto de Física Rosario, Consejo Nacional de Investigaciones Científicas y Técnicas-CONICET, Universidad Nacional de Rosario, Ocampo y Esmeralda, 2000 Rosario, Argentina

[3] Fundació CIM-UPC, c/Llorens i Artigas 12, 08028 Barcelona, Spain

or better hydrogen absorption capacity than in its coarse-grained state [10–12].

Nowadays, numerous plastic deformation techniques have been developed to obtain UFG metallic materials [13]. These techniques are based on the introduction of large amounts of plastic deformation through shear stresses, preferably using closed dies in which the transverse dimensions of the materials are not affected (i.e., are kept constant) [14]. This deformation principle is described as severe plastic deformation (SPD), which allows generating more microstructural transformations than conventional processes due to different deformation modes that lead to a more efficient grain fragmentation. This is because SPD causes significant changes in the texture, breaking preferential orientations and leading to a more random and less intense texture, i.e., low anisotropy [15, 16].

Today, there is a wide variety of processes that use severe plastic deformation to produce UFG materials. The pioneering processes that still stand out today are high-pressure torsion (HPT), accumulative roll bonding (ARB), and equal channel angular pressing (ECAP), on the principles of which other new processes have emerged [17]. These processes are still valid today not only because they allow plastic deformation of metallic materials to large magnitudes (that is, true plastic strains greater than 5) but also because most of them allow obtaining considerable volumes and quality of processed material with respect to other methods used to obtain nanostructured materials, especially those that follow the so-called bottom-up methodology [18].

Since large loads can be involved during processing by SPD techniques such as ECAP, which increase abruptly with changes in the dimensions of the processed parts, the choice of processing parameters (for example, processing path, processing temperature, die geometry, among others) is key to the successful processing of the material. For this reason, the processing of certain materials at room temperature can be more challenging due to their rapid strain hardening capacity, as is the case of austenitic steels [19]. Other materials like titanium and its alloys can be difficult to process due to their limited number of active slip systems at room temperature [20], or even some aluminum alloys due to their alloying elements that make them prone to cracking [21].

Duplex stainless steels (DSS) stand out within stainless steels, characterized by a higher strength and corrosion resistance than austenitic or ferritic stainless steels [22–25]. In addition, these steels have large chromium content (19%–32%), making them resistant to localized corrosion, particularly pitting, and to stress corrosion cracking. These steels are classified into lean, standard, super, and hyper duplex stainless steels based on their alloy content and corrosion resistance [26].

Several investigations have been carried out on DSS in the micrometric and ultrafine state both from the microstructural point of view and its thermal stability and corrosion resistance [2, 27, 28]. However, few of them study the effect of strain hardening, analyzing in detail the behavior and contribution of each phase together with the texture evolution. Thus, it is necessary to establish relationships between the microstructure evolution of each phase, the mechanical response, anisotropy, and processing conditions. For example, Santos et al. [29] studied the strain hardening of a lean duplex stainless steel (LDSS) subjected to cold rolling cycles and subsequent annealing treatments at different temperatures, demonstrating that the effect of transformation induced plasticity (TRIP) of the austenite caused multiple stages of hardening. Continuing with the plastic deformation, Biserova-Tahchieva et al. [30] subjected a super duplex stainless steel to severe plastic deformation using the HPT process to evaluate the effect of nanostructuring on the precipitation of secondary intermetallic phases. The authors found that the combination of SPD with a subsequent heat treatment improved precipitation compared to the material without deformation. In the same way, Llorca-Isern et al. [31] showed that the kinetics of secondary phase nucleation was faster in an super duplex stainless steels (SDSS) than in a DSS. On the other hand, several researchers [32, 33] characterized the stress–strain behavior of a DSS using nanoindentation and microstructure-based finite element tests. They found that α-ferrite (bcc crystal structure) had a slightly higher elastic modulus than γ-austenite (fcc crystal structure), while the latter had a higher average nanohardness and elastic limit than ferrite. Also, Cao et al. [34] studied the microstructural evolution of a DSS subjected to intense plastic deformation through HPT. The authors found that ferrite grains were refined through dislocation activity, while refinement of the austenitic grains was somehow more complicated because of different mechanisms such as twinning, its interaction with dislocations generating de-twinning processes in UFG grains, and subdivision of the twin boundaries. Signorelli et al. [35] analyzed the texture evolution and the grain fragmentation after SPD using the VPSC model and finite elements methods, finding a good correspondence with the experimental data. These methods also predicted the microstructure heterogeneity and grain shape well, proving to be a powerful tool for analyzing the microstructure after SPD processing. Other authors, such as Farias et al. [36], studied the effect of processing speed and subsequent heat treatments on a DSS processed by ECAP. They observed the formation of martensite induced by cold deformation, where the grain boundaries act as preferential sites for recrystallization. Regarding corrosion resistance properties, Ajith et al. [37] showed that the corrosion resistance of a DSS decreases after its processing through 1 ECAP pass.

In consequence, the objective of this manuscript is to quantify the evolution of the microstructure and mechanical properties of a duplex ultrafine grain stainless steel undergoing a SPD process and considering the changes in both phases, ferrite and austenite, their contribution to the overall hardening of

the steel, and the effect of anisotropy. Thus, this study reveals which of the phases is the main responsible for the material strength and anisotropy, allowing to design more efficient DSS. For this reason, the microstructural and texture evolution of each phase was evaluated using electron back-scattering diffraction (EBSD), optical microscopy (OM) uniaxial tensile tests, and crystal plasticity modeling. Thus, relationships were established with the mechanical behavior considering the contribution of each phase and different processing routes on the steel anisotropy.

2 Material and methods

2.1 As-received material

The material selected is a duplex stainless steel (DSS) in the form of 20-mm-diameter and 250-mm-length bars, whose chemical composition is indicated in Table 1. According to Eq. (1) [38], the pitting resistance equivalent number (PREN), which is indicative of the corrosion resistance, is 42.2 for this alloy. Thus, DSS with PREN greater than 40 are classified under super duplex stainless steels (SDSS) [26].

$$PREN = 1(\%Cr) + 3.3(\%Mo + 0.5(\%W)) + 16(\%N) \quad (1)$$

2.2 Severe plastic deformation and mechanical properties

From the as-received bars, samples of 5 mm in diameter and 30 mm in length were machined for subsequent processing by ECAP. In the ECAP process, a die made of BÖHLER S390 steel with internal and external angles of 90° and 30°, respectively, was used, as indicated in Fig. 1a. With this geometry, the strain imposed on the material in each ECAP pass is approximately 1, as indicated by the equation proposed by Iwahashi et al. [39]. The material was processed at 250 °C up to 2 ECAP passes using MoS_2 as a lubricant with a punch feed rate of 1 mm/s. The process was carried out following route A, in which the sample orientation is the same at each pass [40].

The mechanical properties of the materials in both as-received and ECAP-processed conditions were evaluated by hardness and tensile tests at room temperature. Hardness tests were performed with a load of 1 N and a dwell time of 20 s. Two tensile samples for each condition were tested in a Microtest DEBEN machine at a constant crosshead speed of 3.3×10^{-3} mm/s, as indicated in Fig. 1b. Tensile specimens were wire cut in the transverse plane with their length parallel to the extrusion direction (ED). Bone-like samples with gauge dimensions of 4 mm × 1 mm × 1 mm were cut as shown in Fig. 1c.

2.3 Microstructure and texture characterization

The microstructural characterization was carried out using optical microscopy (OM) and scanning electron microscopy (SEM) coupled with the electron back-scattering diffraction (EBSD) technique. The microstructure was observed in the transversal direction (TD) plane (or the plane containing the ED and the normal direction (ND)). First, the surface was prepared by mechanical polishing

Table 1 Chemical composition of the steel (in %wt)

Cr	Mo	N	C	Ni	Mn	P	S	Si	Co	Cu	W	Fe
24.9	3.62	0.27	0.05	6.55	0.53	0.03	0.01	0.62	0.08	0.81	0.66	61.9

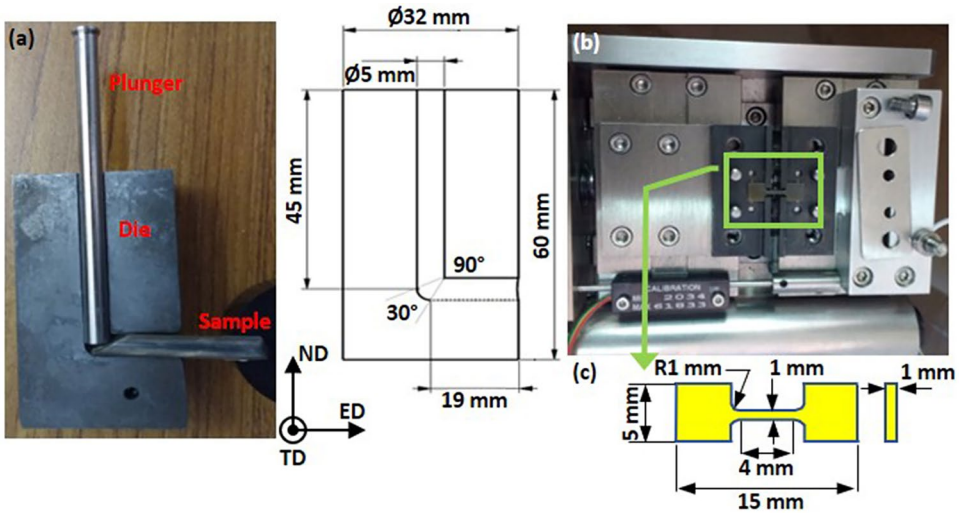

Fig. 1 **a** ECAP die geometry, **b** tensile test machine, and **c** tensile sample dimensions

with SiC sandpaper ranging from 320 to 2500 grit sizes. Subsequently, fine polishing was carried out using diamond suspensions with particle sizes of 9 µm, 3 µm, and 1 µm and colloidal silica with a particle size of 30 nm. Finally, to remove any warping and scratches introduced by mechanical grinding, the surface was electropolished in 30 wt% KOH solution with an etching potential of 2 V for 15 s. EBSD data were acquired using hkl CHANNEL 5 software and processed and analyzed using TSL OIM 7.3b and MTEX toolbox. EBSD maps were acquired with a step size of 1 µm and 30 nm in the as-received and ECAP-processed materials, respectively. Non-indexed points were corrected using the grain dilation method, and grains with less than two pixels were discarded for the statistical analysis. High and low angle grain boundaries were defined as those with misorientations greater than 15° and between 3° and 15°, respectively.

The texture for each phase was calculated using the harmonic series expansion method. On the other hand, geometrically necessary dislocations (GND) were calculated for each phase of the duplex steel from the EBSD maps using the Nye's tensor through whose magnitudes of GND can be obtained by the following equation [41, 42]:

$$GND_{2D} = \frac{1}{b}\sqrt{\alpha_{12}^2 + \alpha_{13}^2 + \alpha_{21}^2 + \alpha_{23}^2 + \alpha_{33}^2} \quad (2)$$

where α represents the components of the Nye's tensor that can be obtained through 2D EBSD maps, b the Burgers vector, which takes values of 2.48×10^{-10} m and 2.51×10^{-10} m for ferrite and austenite, respectively.

2.4 Crystal plasticity modeling

The plastic behavior was studied using the visco-plastic self-consistent (VPSC) model proposed by Lebensohn et al. [43]. Five thousand discrete orientations of equal volume fraction were generated from the texture measured by EBSD for each phase. For slip dislocations, the ($\{111\}\langle 110\rangle$) and 48 ($12\{110\}\langle 111\rangle, 12\{112\}\langle 111\rangle, 24\{123\}\langle 111\rangle$) slip systems for the fcc and bcc structures, respectively, were considered. For the visco-plastic model, a strain rate sensitivity value of $m = 0.05$ was used (a small strain rate sensitivity value was selected considering the deformation process was carried out at temperatures lower than the recrystallization one). The extended Voce law was also used to describe the material hardening as indicated in the following equation [44]:

$$\tau^s = \tau_0^s + \left(\tau_1^s + \theta_1^s \Gamma\right)\left(1 - \exp\left(-\Gamma\left|\frac{\theta_0^s}{\tau_1^s}\right|\right)\right) \quad (3)$$

where $\Gamma = \sum_s \Delta\gamma^s$ is defined as the accumulated shear in the grain, while τ_0, θ_0, θ_1, and $(\tau_0 + \tau_1)$ represent the initial critical resolved shear stress (CRSS), the initial hardening rate, the asymptotic hardening rate, and the back-extrapolated CRSS, respectively. The relationship of these parameters with the stress–strain curve can be found in the research work of Anglin et al. (Fig. 1) [45]. The affine linearization was used for the calculations. The VPSC model was calibrated through the experimental uniaxial tensile curves and texture evolution for each phase at different ECAP passes. To quantify the hardening of each phase (that is, stress and strain partitioning) and to fit the VPSC model into two phases, it was assumed that both phases deform plastically and that the ferrite reached stresses slightly lower than austenite. Hence, a lower τ_0 value was taken for ferrite. This approach has proven successful in describing the plastic behavior of two-phase steels in which each phase has different properties [46]. The initial Voce law values were obtained from reported tensile curves for DSS with a similar composition that analyzes the tensile curves for both phases [32].

The VPSC model allows defining the load orientation concerning the texture coordinate axes. Therefore, the Lankford coefficients evaluated the material anisotropy considering different tensile load orientations in the TD plane concerning the texture data input. For example, to evaluate the Lankford coefficient at 30° concerning the ED, the experimental texture data is rotated around the TD before running the simulation. Then, it is run with the load direction parallel to the laboratory ED axis; thus, there is a 30° angle between the load direction and the texture ED axis.

3 Results and discussion

3.1 As-received and processed materials

Figure 2 summarizes OM images of the as-received and ECAP-processed conditions (1 and 2 ECAP passes) at different magnifications. Figure 2a–c indicate the microstructure of the as-received material, demonstrating the existence of two elongated phases in the ED that are intercalated, giving rise to a banded structure. The two phases correspond to austenite and ferrite, revealed in brown and white, respectively. After the first pass through the ECAP die, as shown in Fig. 2d, the two phases flow through the intersection of the two channels generating changes in their orientation, breaking the perfect banded configuration. This behavior is a consequence of the intense shear deformation introduced by the ECAP process that causes the phases previously oriented towards the ED to change orientation by forming steps with an approximate angle of 50° to regain their initial orientation, as displayed in Fig. 2e, f. With the increase in ECAP

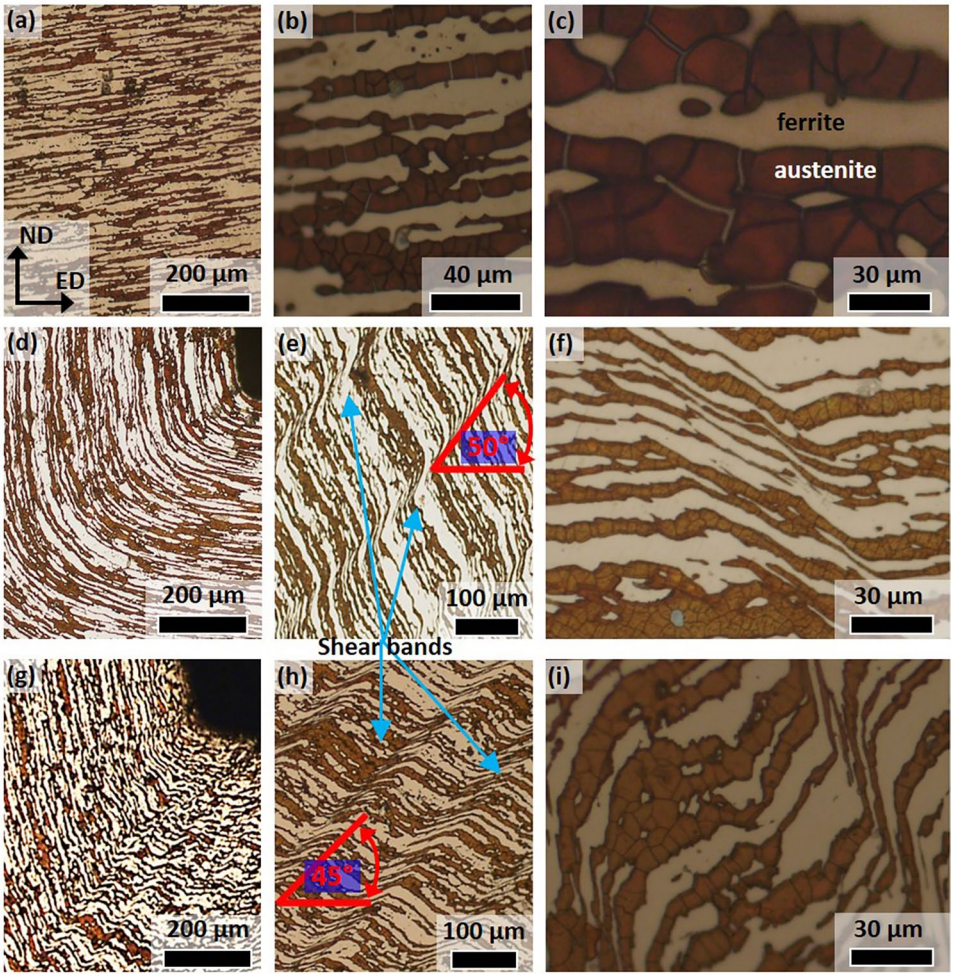

Fig. 2 Optical microstructures at different magnifications for all the materials. **a–c** As-received, **d–f** 1 ECAP pass, and **g–i** 2 ECAP passes

passes, the formation of these steps becomes more evident and repetitive (that is, more steps with less thickness) with an approximate orientation of 45° with respect to ED (see Fig. 2g–i). The repetitive formation of these steps or shear bands that multiply at higher strains while maintaining the same orientation can be attributed to the processing route used, i.e., route *A*, which causes the same deformation plane to be activated by not presenting rotations during repetitive passes.

The appearance of shear bands in high-strength metallic materials such as duplex steels, commercially pure Ti, and twinning induced plasticity (TWIP) steels is a recurrent phenomenon when these materials are subjected to SPD. Several authors attribute this phenomenon to the tendency to localize the deformation, that is, the appearance of plastic instability formed by heterogeneity in the deformation [47, 48]. Besides, the shear bands apparition in the DSS is also related to the different properties of ferrite and austenite. This fact makes the two phases store different magnitudes of deformation, creating a heterogeneous state that favors the appearance of shear bands. This phenomenon has also been shown to be dependent on processing conditions such as temperature, back pressure, strain rate, and, for this particular case, the geometry of the ECAP die [47]. From the microstructural point of view, the formation of shear bands has a marked influence on grain refinement since they are preferential places where new grains of smaller or larger size are formed depending on the initial grain size where they are formed. For example, Su et al. [49] showed that ultrafine grains were formed in shear bands during Ti deformation when the matrix consisted of coarse grains while a combination of coarse and ultrafine grains occurred in shear bands formed on ultrafine grain structures.

3.2 Microstructure and texture

Figure 3 presents different microstructural characteristics measured by EBSD of as-received and processed by ECAP materials. The as-received condition shows an elongated grain structure in the ED for ferrite and austenite (Fig. 3a). After plastic deformation by ECAP, the microstructure changes to more irregular grains, producing a partial break of the lines of grains oriented in the ED, as depicted in Fig. 3b. After 2 ECAP passes, Fig. 3c indicates

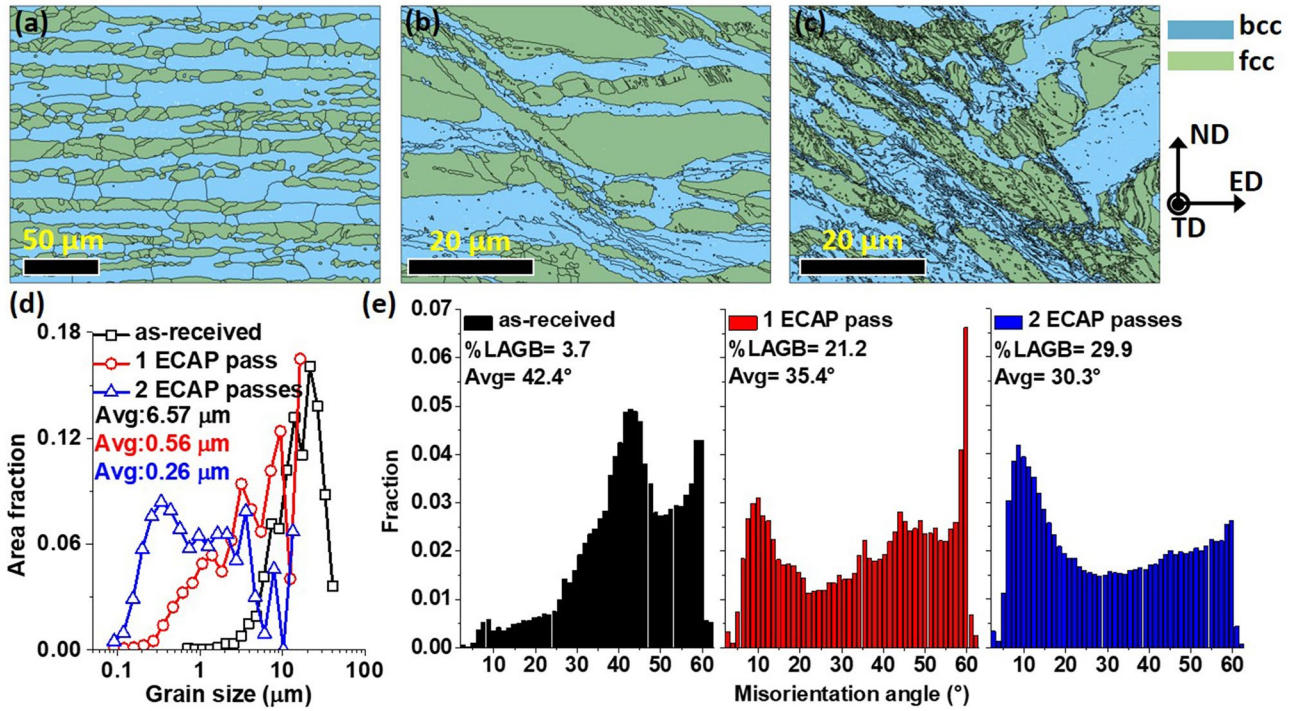

Fig. 3 EBSD characterization. **a** As-received, **b** 1 ECAP pass, **c** 2 ECAP passes, **d** grain size evolution, and **e** misorientation angle distributions

Table 2 LAGB and twinning fractions

Material	LAGB [%]	Twinning [%]
	All material	Austenite
As-received	3.7	18.8
1 ECAP pass	21.2	23.9
2 ECAP passes	29.9	19.9

a more chaotic microstructure where the two phases are mixed with small grains inside the larger ones, especially in the fcc phase, which would show that austenite tends to refine faster than ferrite. Figure 3d demonstrates how ECAP processing results in a considerable grain refinement going from an average grain size of 6.57 µm in the as-received condition to 0.26 µm after two ECAP passes, representing a reduction of more than one order of magnitude, going from the micrometric to the ultrafine range with sizes that can reach 200 nm. The faster grain refinement in austenite can be attributed to the twinning deformation mechanism, which favors grain fragmentation. Table 2 shows that after ECAP processing, the twinning fraction increments reach 27% after one ECAP pass. The main observed twins were 60° ⟨111⟩ and 38° ⟨110⟩ types related to material recrystallization. Besides, it is worth mentioning that at the ECAP processing temperature, the austenite/ferrite ratio did not change, suggesting no martensitic transformation, whereby the responsible mechanisms of grain fragmentation in austenite are the interactions between dislocations (dislocations pile up) and dislocations-twins (dynamic Hall–Petch effect).

As in many other metallic materials subjected to SPD, grain refinement results from the creation and grouping of dislocations that allow the generation of new grain boundaries, as shown in Fig. 3e and Table 2. This figure shows how ECAP deformation increases the fraction of low angle grain boundaries (LAGB) reaching 21% and 30% fractions after 1 and 2 ECAP passes. Several authors have established that this behavior obeys the continuous dynamic recrystallization (CDRX) phenomena [50–54]. In this mechanism, new grain boundaries are generated from dislocation walls, which can evolve into high angle grain boundaries (HAGB), increasing their misorientation by absorbing more dislocations giving rise to small grains without nucleation as traditionally observed in the discontinuous dynamic recrystallization (DDRX).

The nature change of the grain boundaries is consistent with the grains' preferential orientation change as indicated in Fig. 4 by the texture represented in the pole figures {110} and {111} for both as-received and ECAP-processed materials. Thus, Fig. 4a indicates that in the as-received condition the material presents a typical extrusion or lamination texture found in metallic materials produced as bars or plates [50, 54]. After the first and second ECAP passes, Fig. 4b–d indicate a rotation of the texture around the TD, generating simple-shear texture components for the two phases. This behavior proves that the effect of shear deformation leads to

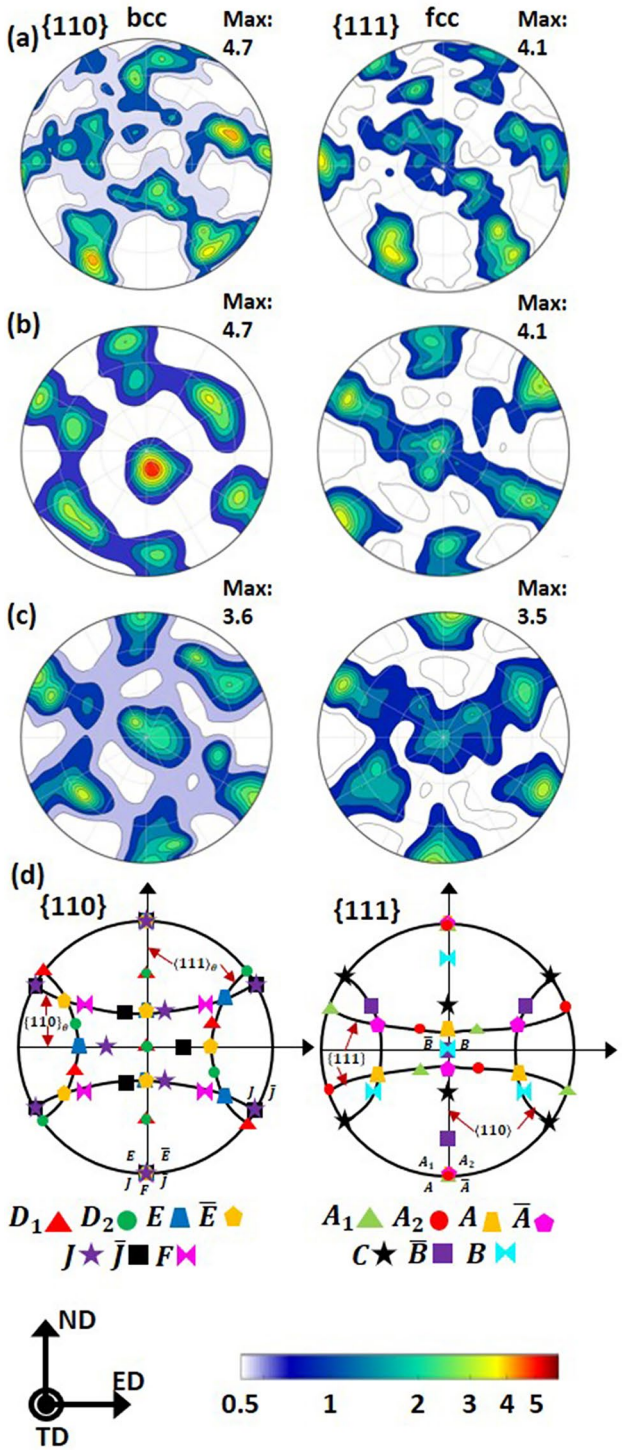

Fig. 4 Texture evolution for all the materials and phases. **a** As-received, **b** 1 ECAP pass, **c** 2 ECAP passes, and **d** simple shear ideal orientations for bcc and fcc structures

a faster and more remarkable grain refinement than monotonic deformation processes, such as conventional rolling and extrusion due to the rotation of the grains and subsequent fragmentation.

3.3 Mechanical properties

The tensile behavior and hardness of the ECAP-processed and as-received material are illustrated in Fig. 5. After 1 ECAP pass, the material shows a 39% increase in yield strength accompanied by a marked reduction in the elongation to fracture and in the homogeneous deformation zone with values of 52% and 88%, respectively, as displayed in Fig. 5a. The low ductility in metallic materials processed by SPD techniques is related to the microstructural properties of UFG materials in which the grain size refinement gives rise to less space for the free movement of dislocations which in turns limit the strain hardening capacity of the material due to an increase in the annihilation rate of dislocations [55, 56]. This causes the plastic instabilities to appear quickly under a monotonic tensile test, locating the deformation and its prompt fracture. In this sense, Fig. 5b compares the hardening rate for the samples in the as-received and ECAP-processed by 1 pass conditions. Although the material processed by ECAP reaches higher strain hardening values, its decay is much more abrupt than the as-received material, as shown by the higher value of the Hollomon exponent in Fig. 5a. This fact means that the extension of the homogeneous hardening zone is more significant in the as-received material according to the Considère criterion (that is, plastic instability begins when the rate of strain hardening is less than or equal to the yield stress, $d\sigma/d\varepsilon \leq \sigma$ [57]). This is because the micrometric grain size of the as-received material offers a larger mean free-path for the motion of a lower dislocation density than the processed material. It is worth mentioning that in the hardening curve of the ECAP-processed material, different steps are observed before the plastic instability, which can be related to the multiple shear bands generated by the ECAP process in the microstructure, as indicated in Fig. 2. This observation is possibly correlated with the deformation partition between both phases, which gives rise to a heterogeneous state in which larger deformations are assumed by one the phases.

Additionally, Fig. 5c shows that the duplex steel hardness increases with the number of ECAP passes, although the increase is reduced between consecutive passes at higher strains; for example, after the first ECAP pass, the increase is 23%, while after the second pass it is 9.6%. This behavior towards saturation in material hardening can be associated with a change in the deformation mechanism. At large strains, dislocation slip effectiveness ceases and the activation of hardening by slip and rotation of grain boundaries after huge strains is expected [22, 58].

3.4 Ferrite and austenite contributions

In the quest to better understand the response of each phase in the steel to the deformation, Fig. 6a indicates the

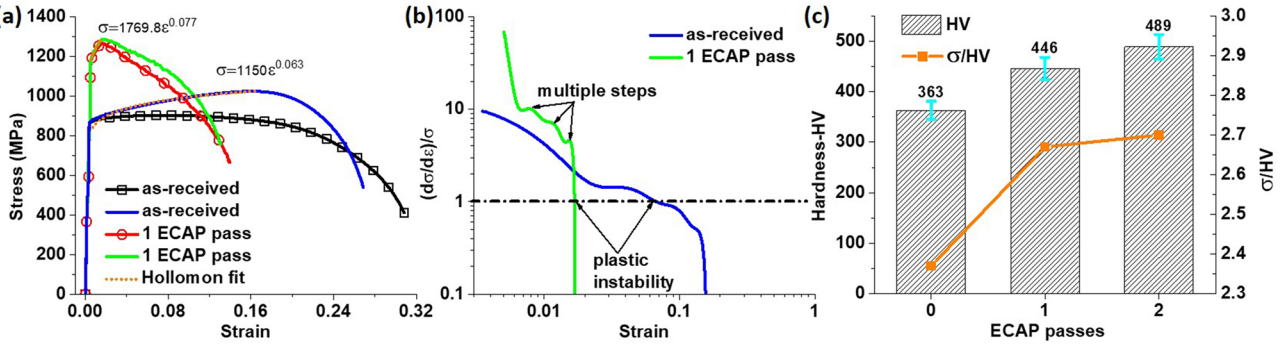

Fig. 5 Mechanical properties for all the materials. **a** Tensile curves for the as-received and 1 ECAP pass materials (solid and symbol lines correspond with the true stress–strain and engineering stress–strain curves, respectively). **b** Strain hardening curves for the as-received and 1 ECAP pass materials. **c** Yield strength-hardness ratio

misorientation angle distributions for each phase at different processing conditions. It is evident in the as-received condition that there are apparent differences in the grain boundary fractions between the ferrite and the austenite phases. For example, ferrite has a higher LAGB fraction than austenite, with 19.3% and 4.1%, respectively. After ECAP processing, the LAGB fraction increases in ferrite, reaching 34.7% after two passes, while a significant increase occurs in austenite, going from 4.1% to 28.1%. This behavior suggests that ferrite has a greater capacity than austenite to accumulate GND since part of these dislocations accumulates in LAGB [41, 59]. In addition, using the grain reference orientation deviation (GROD) maps obtained through EBSD, it is possible to appreciate zones inside the grains where there are deformation heterogeneities and higher concentrations of dislocations [60, 61]. As a first observation, the maps in Fig. 6b–d suggest higher GROD values with the deformation going from an average of 25.4° in the as-received state to

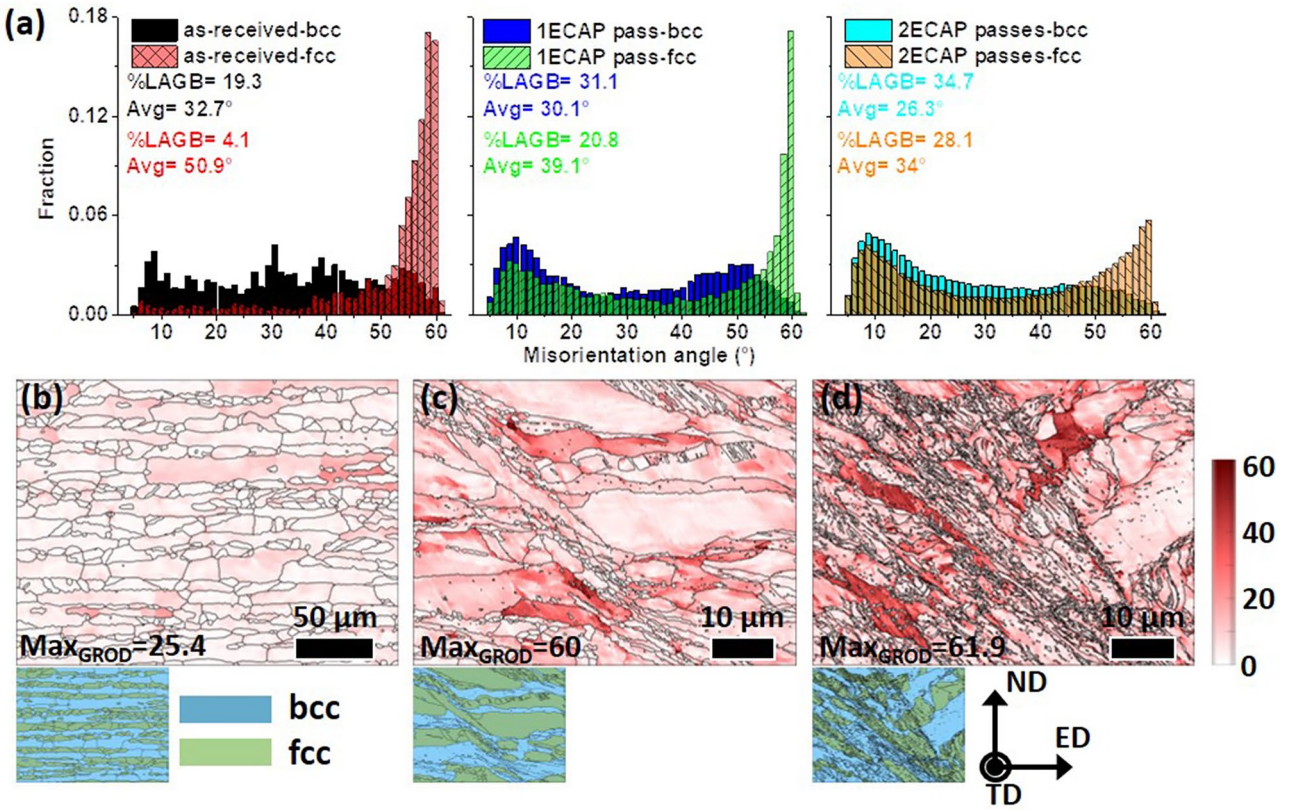

Fig. 6 **a** Misorientation angle distributions for each phase, and GROD maps for the **b** as-received, **c** 1 ECAP pass, and **d** 2 ECAP pass materials

values greater than 60° after ECAP processing, indicating more deformed microstructures. However, it stands out that the highest GROD values are found inside the ferrite grains, corroborating that this phase presents greater heterogeneities and higher dislocation densities than austenite. On the other hand, although the GROD values are lower in the austenite than ferrite, the behavior is also heterogeneous, although to a lesser degree.

The behaviors previously described in Fig. 6 allow evaluating that ferrite is the phase with more defects, suggesting that it is the more affected phase by the SPD process. In this sense, these microstructural changes can be better understood from the energy stored in the grain boundaries through the Read-Shockley equation [62]:

$$\gamma(\theta) = \begin{cases} \gamma_m\left(\frac{\theta}{\theta_m}\right)\left[1 - ln\left(\frac{\theta}{\theta_m}\right)\right]; \; if \; \theta < \theta_m \\ \gamma_m; \; if \; \theta > \theta_m \end{cases} \tag{4}$$

where $\gamma(\theta)$ is the energy for a given misorientation, γ_m= 0.617 Jm^{-2} is the energy per unit area of a HAGB, θ represents the different values of misorientation, and θ_m= 15° represents the misorientation threshold above which the energy per unit area is independent of the angle of misorientation. Therefore, the average energy for each phase can be obtained by adding the contributions at different angles of misorientation as indicated by the following equation [63]:

$$\overline{\gamma} = \begin{cases} \sum_2^{62.8}\left[\gamma(\theta)f(\theta)\right]; \text{ ferrite} \\ \sum_2^{63.5}\left[\gamma(\theta)f(\theta)\right]; \text{ austenite} \end{cases} \tag{5}$$

where $f(\theta)$ is the fraction of grain boundaries for a given misorientation. Therefore, the energy stored in the grain boundaries can be calculated using the following equation [64]:

$$E_b = \frac{2\overline{\gamma}}{d_{\text{subgrain}}} \tag{6}$$

where d_{subgrain} is the average grain size of subgrains. Therefore, it is possible to obtain the energies stored in the grain boundaries for each phase at different ECAP passes using Eqs. (4) to (6) and the data obtained through the EBSD maps as indicated in Table 3. The stored energy in the boundaries indicates a direct relationship with the deformation. It increased notably in the two phases, going from values of the order of 0.93 J/mol in the as-received condition up to 34.06 J/mol after two ECAP passes. In addition, it is highlighted that the increases in austenite are greater than those of ferrite. Thus, the energies corroborate a higher grain refinement with the HAGB domain due to a higher degree of recrystallization in austenite than ferrite.

On the other hand, to better understand the mechanisms of grain fragmentation generated by ECAP, the misorientation axis distributions (MAD) for both phases are displayed in Fig. 7. It can be seen that the as-received material in Fig. 7a splits the highest MAD intensities along the ED, demonstrating that the conventional extrusion used to produce bars generates grain refinement through boundary fragmentation with MAD parallel to the ED. However, when the deformation mode is dominated by shear strain like in ECAP, as demonstrated by texture and microstructure changes in Figs. 2 and 4, grain fragmentation during the first ECAP pass occurs with a MAD close to TD as suggested by Fig. 7b. At higher strains, the 2 ECAP passes material indicates an overall drop in MAD intensity in Fig. 7c, where the high intensities are localized between TD and ED and another concentration between ND and ED. These observations demonstrate that both phases follow a similar path for grain fragmentation, although it does not mean both phases' grain boundaries fragment at the same time and rate.

Figure 8 shows the evolution of GND for the different materials considering both phases, which also helps to evaluate the microstructural fragmentation behavior. GNDs play a fundamental role in plastically deformed polycrystalline metallic materials since they can offer hardening by generating short-range back-stresses [60]. In Fig. 8a–c, the GND maps demonstrate obvious differences between the material received and after ECAP processing. At first glance, it stands out that there are not many groups of GND forming walls in the as-received condition, except in some boundaries observed inside the ferrite grains. On the other hand, in the ECAP-processed material, Fig. 8b and c show that both phases present walls or groups of dislocations inside the grains. This behavior is due to grain size reduction in which the original grains experience an intense shear deformation that generates significant changes in their curvature. In this way, GNDs are generated to compensate for the change in curvature. GNDs also explain how non-monotonic processes such as ECAP allow more prominent grain refinements to be

Table 3 Microstructure properties and grain boundaries energy

Material	Grain size [μm]		Subgrain size [μm]		$\overline{\gamma}$[J/m^2]		E_b [J/mol]]	
	Ferrite	Austenite	Ferrite	Austenite	Ferrite	Austenite	Ferrite	Austenite
As-received	11.77	6.19	9.12	5.45	0.6	0.61	0.93	1.59
1 ECAP pass	0.99	0.67	0.66	0.49	0.6	0.61	12.90	17.67
2 ECAP passes	0.37	0.32	0.27	0.25	0.59	0.6	31.01	34.06

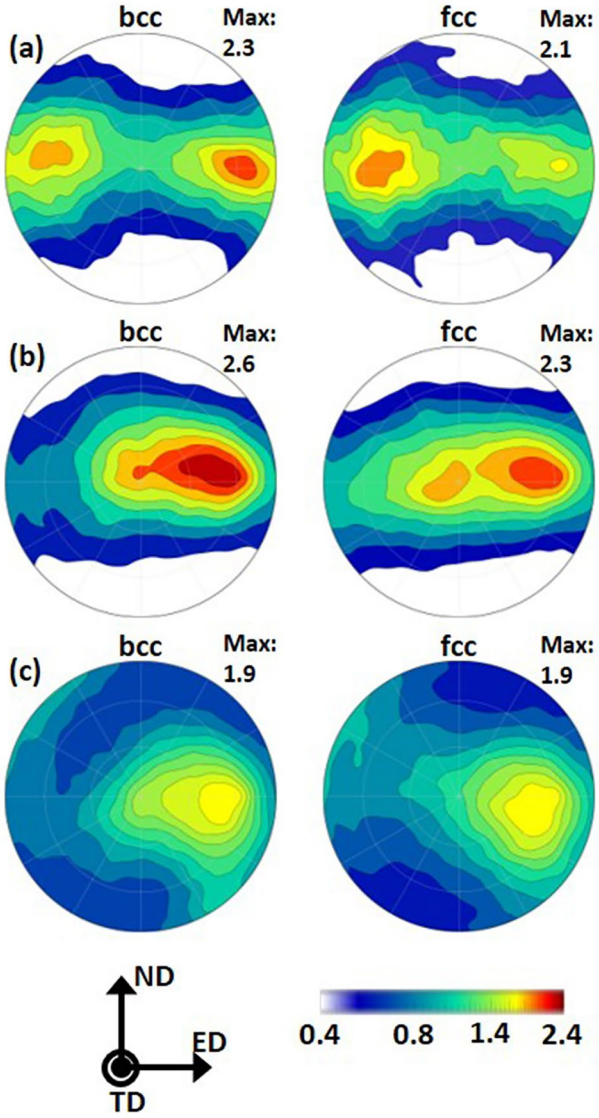

Fig. 7 Misorientation axis distributions for the **a** as-received, **b** 1 ECAP pass, and **c** 2 ECAP pass materials

achieved, generating substantial texture changes, than monotonic ones such as a conventional extrusion (the one in which the material was supplied).

The effect of the two deformation processes, i.e., extrusion and ECAP, is demonstrated by the magnitudes of the GNDs indicated in the distributions in Fig. 8d. These distributions show that the mean value of GND increases by one order of magnitude after ECAP processing for both phases compared to the as-received material. However, the magnitude of GND does not change substantially after the second ECAP pass compared to the single ECAP pass material. This behavior is consistent with the saturation reached in different microstructural characteristics of metallic materials subjected to SPD. The most abrupt changes in dislocation density and grain sizes occur in the initial stages; then, at high plastic deformations, most of the microstructural changes are reduced, reaching the Hall–Petch limits [65, 66]. However, different behaviors are observed when analyzing the GND configurations inside the grains for each phase in detail, as indicated in Fig. 8e. For example, the GND profiles of the as-received condition display some minor differences, with more peaks in the ferrite than in the austenite. This behavior becomes more evident after 1 ECAP pass where the ferrite presents multiple GND variations with respect to the austenite represented by multiple peaks that reach maximums and minimums. After the second ECAP pass, the austenite also shows a saw-tooth behavior, although the ferrite still shows the widest variations. This behavior suggests that the GND are grouped in the ferrite, forming walls, while the GND seem to be more homogeneously distributed in the austenite. This shows that the ferrite would be hardening faster than the austenite, and its grain size is reducing faster. On the other hand, the formation of plastic gradients within the ferrite and between the two phases is also confirmed. According to Calcagnotto et al. [67], ferrite develops heterogeneous GND distributions in dual-phase steels. Therefore, the way GNDs are configurated demonstrates the back-stress development between the two phases due to the tension exerted by the toughest phase on the softest. For that reason, to compensate the tension differences between ferrite and austenite, GNDs pile up in the ferrite.

3.5 Hardening contributions

Figure 9a indicates the grain size evolution for each phase at different deformation magnitudes. Initially, it is verified that the average grain size of the as-received material for the two phases is different, being austenite grains smaller than ferrite with values of 5.45 μm and 9.12 μm, respectively. This behavior is maintained even after two ECAP passes, although the differences become smaller at increasing strain. Thus, the ferrite, which has a larger initial grain size, undergoes a higher degree of microstructure fragmentation (i.e., ferrite has a higher ability to recrystallize continuously) than austenite, as shown by the LAGB fractions and dislocation configuration through GROD and GND calculations. On the other hand, the smaller grain sizes in austenite show that this phase contributes a little more to the overall hardening of the material according to the Hall–Petch equation [68, 69]:

$$\sigma_y = \sigma_0 + k_{HP} d^{-1/2} \tag{7}$$

where σ_y is the yield strength of the material, σ_0 is the friction stress, k_{HP} is a constant, and d is the average grain size. Thus, Fig. 9b indicates a Hall–Petch plot considering the grain size of all the material at different ECAP passes.

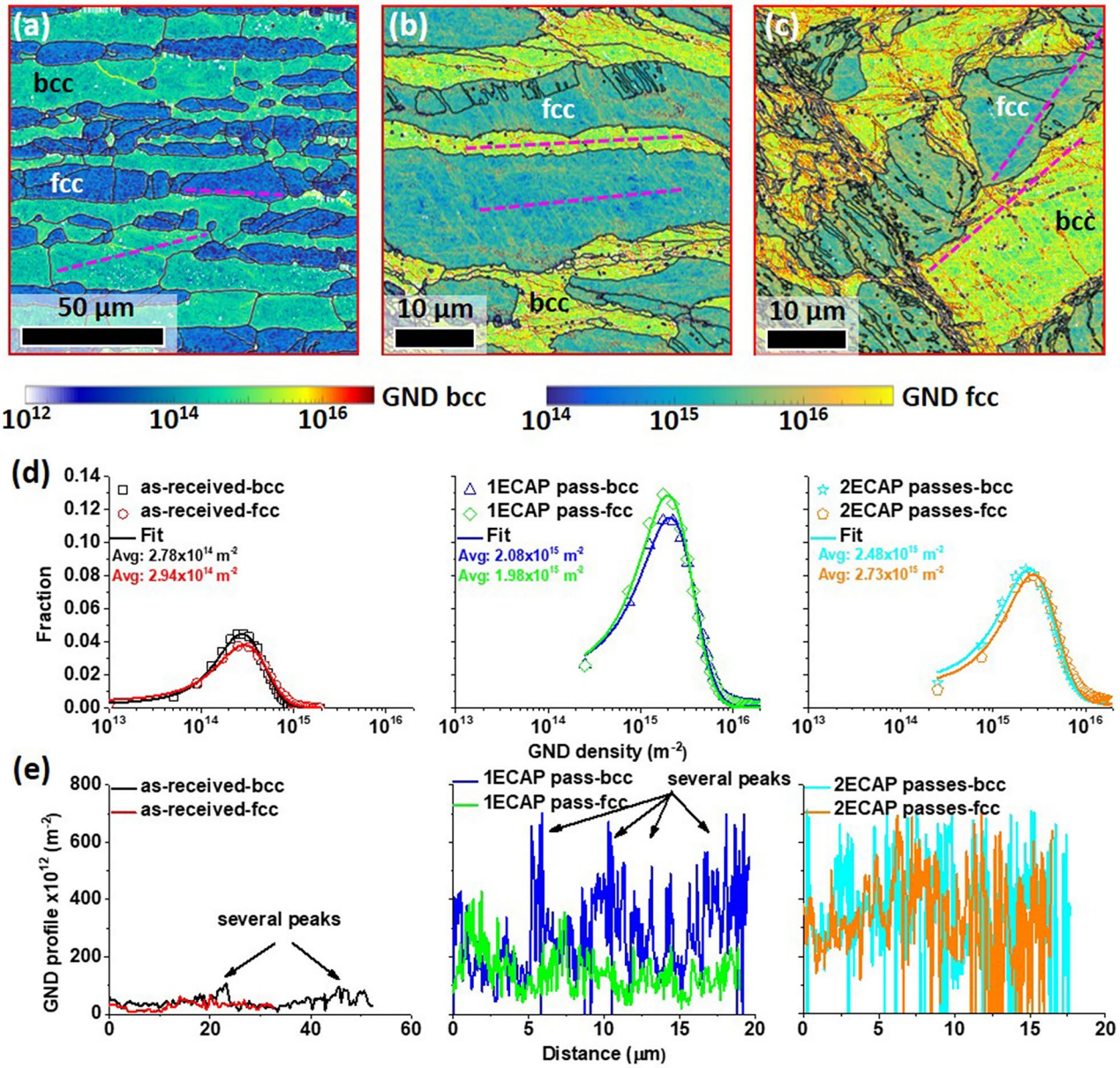

Fig. 8 GND maps for the **a** as-received, **b** 1 ECAP pass, **c** 2 ECAP passes materials, **d** GND distributions for each phase and studied material, and **e** GND profiles (pink dashed lines on GND maps)

The experimental data fit Eq. (7) very well, indicating a σ_0= 758 MPa and a Hall–Petch hardening constant k_{HP}= 298.4 MPa/µm$^{1/2}$. Therefore, when plotting the grain sizes for each phase on the straight line, it can be verified that austenite reaches higher strengths than ferrite. However, it would be a first approximation since the strength of each phase should not necessarily be on the Hall–Petch line calculated as a single-phase material.

To better understand the contributions of each phase, through the simulations of the VPSC model, the tensile curves of each phase were obtained at different magnitudes of deformation, as indicated in Fig. 10. In the as-received condition, Fig. 10a shows that ferrite behaves in a less-strength way but is more ductile than austenite which in turns provides strength to the material. This behavior is repeated in the material with 1 ECAP pass as indicated in Fig. 10b, although with marked reductions in ductility due to the drastic change in the material's microstructure. The curves predicted for each phase by the VPSC model show a good correspondence with curves reported from nanoindentation and finite element tests for duplex stainless steel as in the work of Tao et al. [32]. This behavior corroborates what was previously stated using the Hall–Petch equation in which austenite provided greater

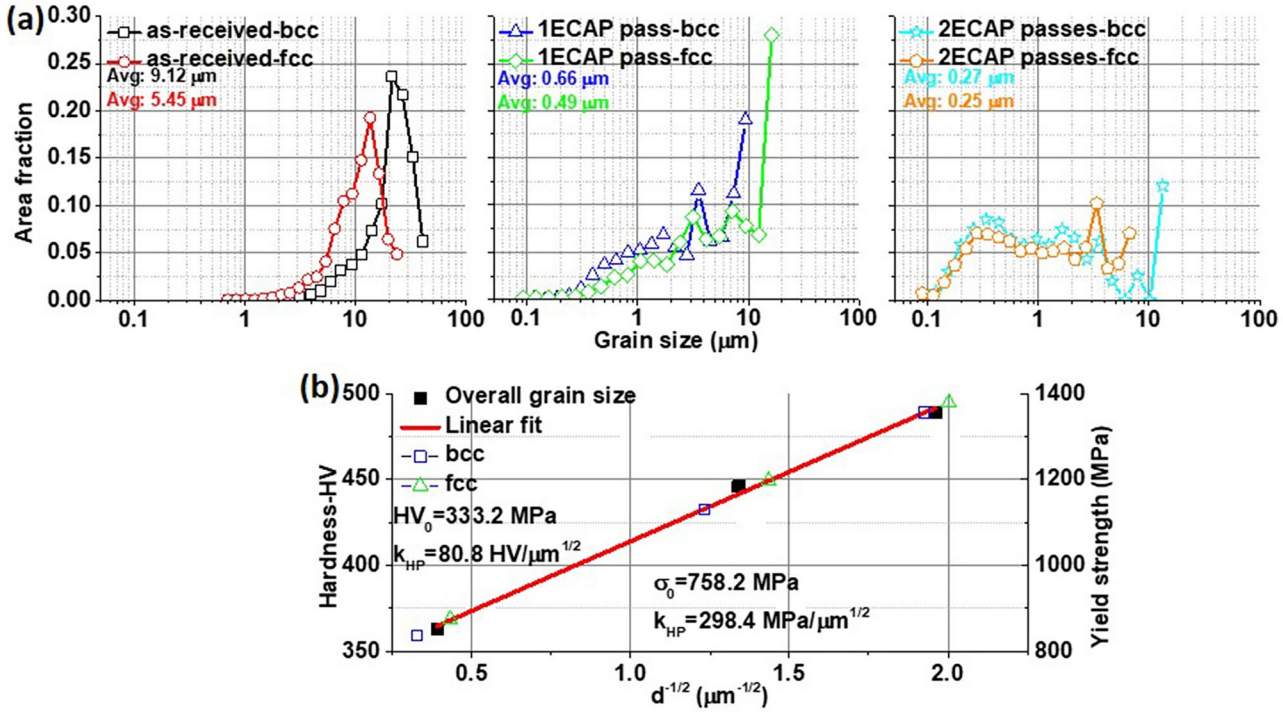

Fig. 9 **a** Grain size evolution for each phase after different processing conditions. **b** Hall–Petch plot

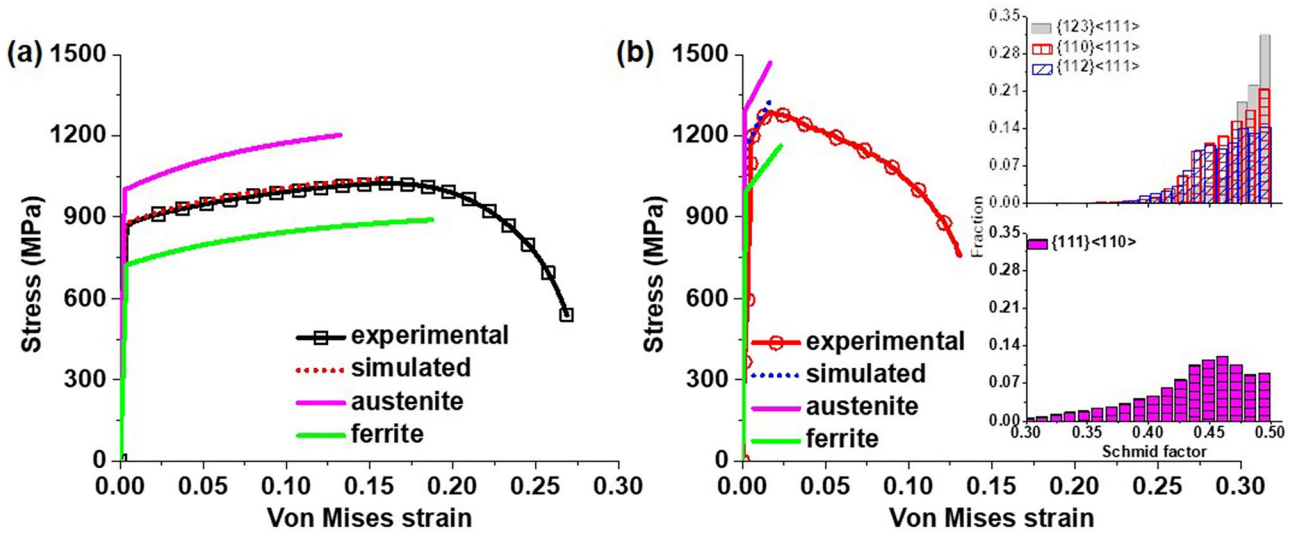

Fig. 10 Austenite and ferrite contributions during the tensile tests for the **a** as-received and **b** 1 ECAP pass materials together with the experimental Schmid factors

strength and, at the same time, shows that the strengths of each phase separately do not lie on the same global material line. Figure 10b also shows the evolution of the Schmid factor for the material with 1 ECAP pass considering both phases and their different slip systems. This inset allows to observe that the Schmid factors of the ferrite are higher than in the austenite, with the system $\{123\}\langle111\rangle$ being the one with the highest values and close to 0.5. This suggests that although the ductility of the DSS is penalized by the SPD, its plastic behavior still suggests a good performance, possibly accepting higher magnitudes of plastic deformation without fracture.

Through the VPSC model, it is also possible to predict the strength contribution of each phase throughout the ECAP process at different numbers of ECAP passes, as shown in Fig. 11a. In this figure, it can be seen that the VPSC model correctly predicts the strength curve of the process and the texture of both phases represented as pole figures that are very similar to those described in Fig. 4. The yield strength curves again indicate that austenite provides higher hardness, as evidenced by the higher strengths and the steeper curve shape. In contrast, although the ferrite curve reaches saturation faster than austenite, it stores more strain. Furthermore, it is worth mentioning that between the two phases, there is also a strain partition in which ferrite reaches higher strains than austenite. This behavior is related to the heterogeneous grouping of GND between the two phases and the twinning hardening, confirming the back-stress effect indicated in Fig. 8 (i.e., more GNDs piled up on the soft than the hard phase), which has been reported in materials with two phases and with heterogeneous structures of the harmonic type where there is additional hardening by the hetero-deformation [70, 71]. Furthermore, finding different microstructural and mechanical behaviors between the two phases is well related to the slip activity indicated in Fig. 11b. This figure shows that austenite has a higher slip activity than ferrite where the slip system $\{123\}\langle 111\rangle$ is the most active one while the $\{110\}\langle 111\rangle$ is the one that is most activated with deformation. This is due to the development of texture components in fibers $\{111\}$ and $\{110\}$ for austenite and ferrite after ECAP processing, respectively.

By knowing the strength curves for each phase, its hardening capacity can be evaluated, as illustrated in Fig. 11c. This graph shows that the material rapidly reduces the strain hardening capacity in its initial stage to reach a steady state and decrease again. For austenite, it is observed that after the initial decay, this phase presents a longer and more defined plateau than ferrite without reaching zero rates. On the contrary, although ferrite reaches higher hardening rates at the beginning of the deformation, its decay is the most pronounced. However, the ferrite strain hardening rate curve extends to the largest deformations. These results confirm the fact that under the current processing conditions, the DSS cannot be processed for more than 2 ECAP passes without fracturing since the three strain hardening curves report the occurrence of plastic instability as suggested by the Considère criterion (i.e., instability occurs when $^{d\sigma}/_{d\varepsilon} \leq \sigma$) [57]. Additionally, the differences in the strain hardening curves for the two phases are related to the way the dislocations are ordered, giving rise to shear bands in the material because each phase hardens differently. Moreover, the twinning induces plasticity (TWIP) effect

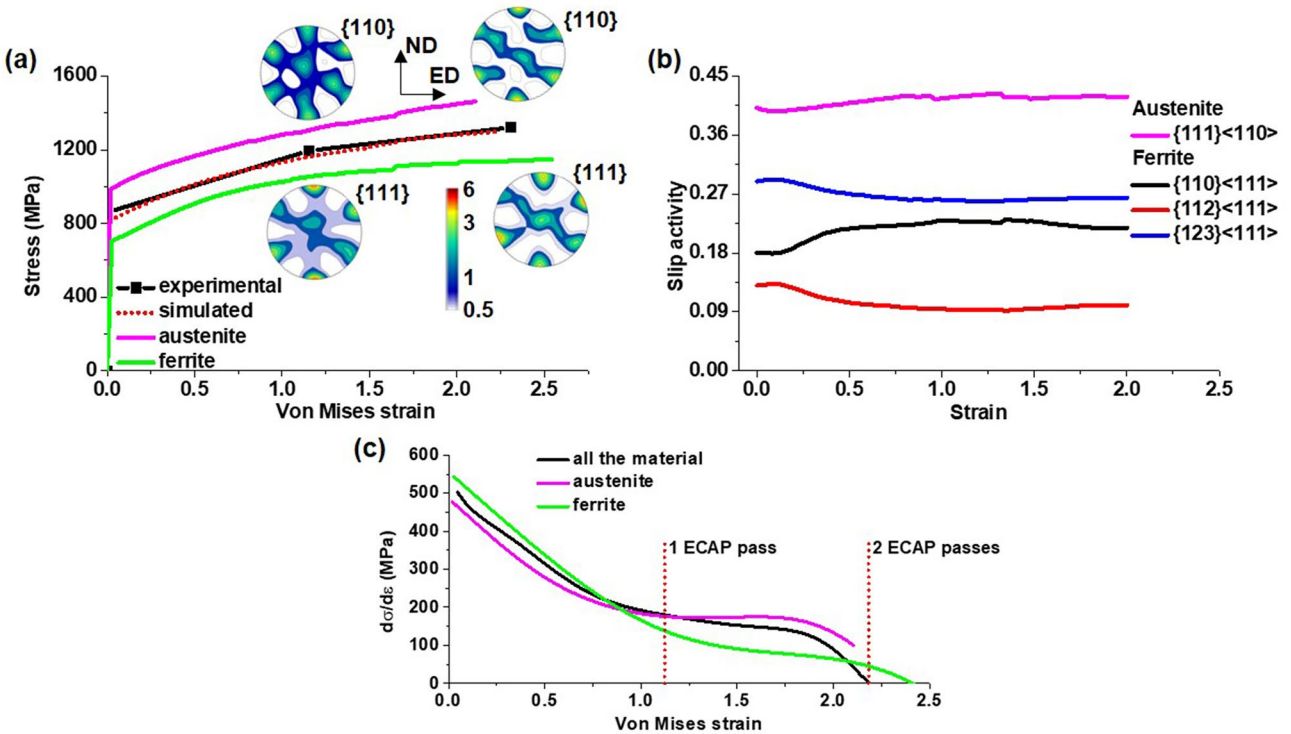

Fig. 11 VPSC simulations for the ECAP curve. **a** Austenite and ferrite contributions during the ECAP process. **b** Slip activity during the ECAP process. **c** Strain hardening curves for each phase during the ECAP processing

generated in austenite can be responsible for its lower strain hardening rate decrease.

Hence, knowing the contributions of each phase of the duplex steel, the overall material strength can be expressed by an equation that describes its yield strength through a modified Hall–Petch equation that considers each phase, as well as its fraction as indicated below:

$$\sigma_y = f_{\text{fer}}\left(\sigma_{0-\text{fer}} + k_{\text{HP}-\text{fer}} d_{\text{fer}}^{-1/2}\right) + f_{\text{aust}}\left(\sigma_{0-\text{aust}} + k_{\text{HP}-\text{aust}} d_{\text{aust}}^{-1/2}\right) \quad (8)$$

with f_{fer} and f_{aust} as the ferrite and austenite fractions, respectively.

Thus, Fig. 12 plots the whole grain size values against strength after different number of passes as indicated in Fig. 9b and the Hall–Petch curves for each phase considering its grain size and the strengths predicted by the VPSC model according to Fig. 11a. Through the adjustments of each phase to the Hall–Petch equation, it can be shown that the strength of duplex steel can be described by the weighted equation (Eq. (8)) that considers the contribution of each phase as shown by the comparison of the experimental and theoretical values in Table 4. Additionally, from Eq. (8), different behaviors can also be predicted for different percentages of phases. For example, the largest the austenite content, the highest the material strength. Therefore, to design more efficient steel, it can be argued that if ductility prevails, higher concentrations of ferrite should be involved. Conversely, if greater strength is sought, the percentage of austenite should be increased.

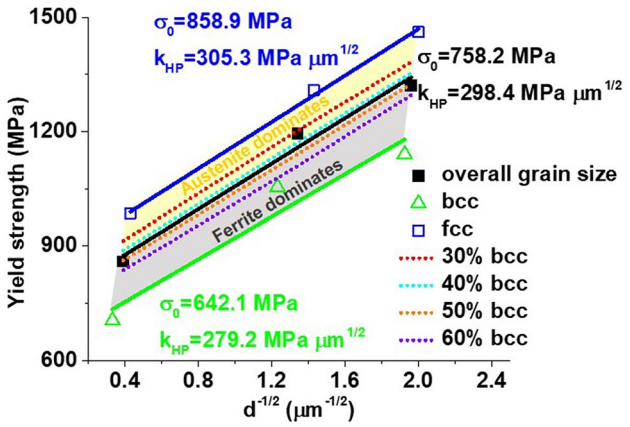

Fig. 12 Hall–Petch equation predictions

Finally, through the VPSC model simulations, the mechanical anisotropy of the steel was evaluated by quantifying the values of average normal anisotropy ($\bar{r}$) and planar anisotropy (Δr) obtained through the following equations [8]:

$$\bar{r} = \frac{r_0 + 2r_{45} + r_{90}}{4} \quad (9)$$

$$\Delta r = \frac{r_0 - 2r_{45} + r_{90}}{2} \quad (10)$$

where r_0, r_{45}, and r_{90} represent the Lankford coefficients for different angles concerning the ED.

Thus, Fig. 13 presents the variation of the Lankford coefficients for different ECAP passes considering processing paths A and B_C (the sample is rotated 90° around its longitudinal axis between each ECAP pass, always maintaining the same direction). In this figure, after the first ECAP pass, the planar anisotropy is reduced while the value of $\bar{r}$ increases. After 2 ECAP passes, both $\bar{r}$ and Δr values increased. This behavior can be attributed to the drastic change in the microstructure generated by the rotation and fragmentation of the original grains that, as mentioned above, give rise to heterogeneous behavior between the two phases. For example, high LAGB in ferrite while the presence of HAGB dominates in austenite as well as the different dislocation configurations in each phase. Therefore, it would be expected that after several ECAP passes (i.e., a more homogeneous microstructure dominated by HAGB), the steel anisotropy could be significantly reduced.

Based on the results indicated in Fig. 10, we also evaluated the anisotropy behavior for each phase, as shown in Fig. 14. At first glance, we can observe that after ECAP processing, the planar anisotropy is higher in austenite than in ferrite, while the oppositive happens in the as-received material. However, as the deformation progresses, the planar anisotropy differences between phases decrease, but the average normal anisotropy values increase concerning the as-received condition. Thus, the DSS, after processing by ECAP, owes its strength and ductility to the austenite and ferrite phases, respectively.

Table 4 Parameters and constants of the modified Hall-Petch equation

Material	k_{HP} [MPa μm$^{1/2}$]		Phases [%]		σ_y experimental [MPa]	σ_y Eq. (8) [MPa]
	Ferrite	Austenite	Ferrite	Austenite		
As-received	279.2	305.3	0.58	0.42	860.0	841.7
1 ECAP pass	279.2	305.3	0.58	0.42	1195.0	1115.7
2 ECAP passes	279.2	305.3	0.58	0.42	1320.8	1301.3

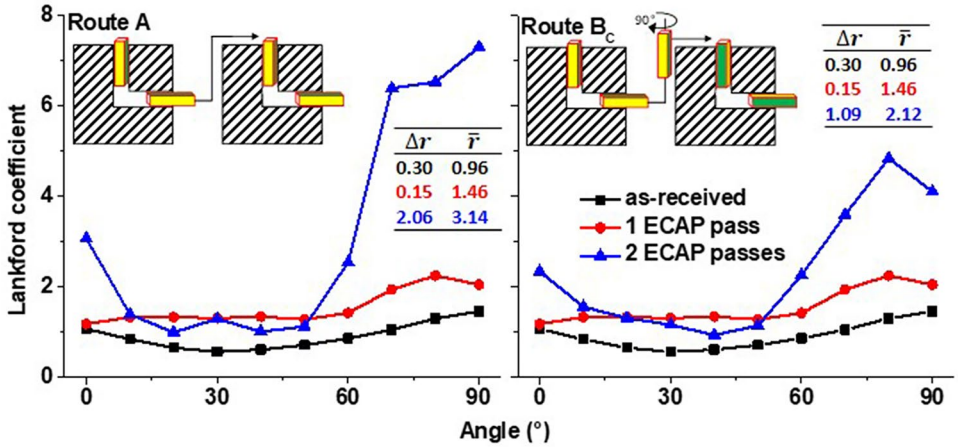

Fig. 13 Lankford coefficients for different ECAP passes considering two processing routes

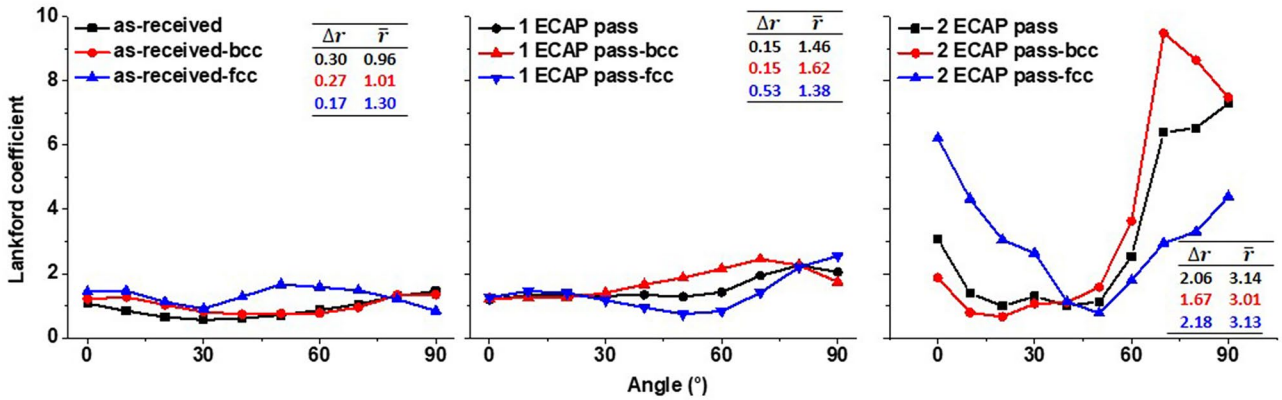

Fig. 14 Lankford coefficients for each phase after different ECAP passes

Furthermore, the austenite seems more responsible for the planar anisotropy increments after 2 ECAP passes than the ferrite.

4 Conclusions

The processing of duplex stainless steel by ECAP up to a true plastic strain of 2 and the subsequent study of the microstructural evolution and the mechanical behavior allowed the following conclusions to be drawn:

1. Severe plastic deformation of a duplex stainless steel with 58% volume fraction of austenite and 42% ferrite gave rise to the formation of shear bands in the material's microstructure on which ultrafine grains were formed with the prevalence of LAGB and HAGB in ferrite and austenite, respectively.
2. The shear deformation generated a heterogeneous behavior in the distribution of dislocations within the steel phases. It was found by EBSD that there was a more significant misorientation spread generating a grouping of GND in walls within the ferrite grains. Contrarily, the dislocations were more uniformly distributed in the austenite, demonstrating a mechanism of heterogeneous strain hardening, and consequently strain partition.
3. The crystal plasticity modeling showed that austenite provided strength to the DSS because of the dislocations and twinning hardening while ferrite assumed large strains. Thus, it was shown that ferrite reaches plastic instability faster than austenite. At the same time, the simulations indicated an increase in anisotropy during the first two ECAP passes associated with the strain partitioning and the well-differentiated microstructural characteristics between ferrite and austenite. Thus, it was also shown that austenite registered larger planar anisotropy values than ferrite after 2 ECAP passes.
4. From the Hall–Petch equation and the application of the VPSC model, it was possible to generate a composite equation based on the rule of mixtures that describes the DSS strength. This equation considers the percent-

age of phases and can be used to describe the behavior of duplex stainless steels with different percentages of ferrite and austenite. Therefore, the more austenite, the stronger, and the larger the planar anisotropy in the steel.

Author contribution All authors contributed to the study conception and design. Material preparation, data collection, and analysis were performed by Jairo Alberto Muñoz, Mohan Chand, Javier Walter Signorelli, Jessica Calvo, and José María Cabrera. The first draft of the manuscript was written by Jairo Alberto Muñoz, and all authors commented on previous versions of the manuscript. All authors read and approved the final manuscript.

Funding Open Access funding provided thanks to the CRUE-CSIC agreement with Springer Nature.

Data availability The raw/processed data required to reproduce these findings cannot be shared at this time as the data also forms part of an ongoing study.

Code availability The VPSC code is available upon request to the original authors.

Declarations

Ethics approval Not applicable.

Consent to participate Not applicable.

Consent for publication Not applicable.

Competing interests The authors declare no competing interests.

References

1. Renton NC, Elhoud AM, Deans WF (2011) Effect of plastic deformation on the corrosion behavior of a super-duplex stainless steel. J Mater Eng Perform 20:436–444. https://doi.org/10.1007/s11665-010-9688-z
2. Tavares SSM, da Silva MR, Pardal JM, Abreu HFG, Gomes AM (2006) Microstructural changes produced by plastic deformation in the UNS S31803 duplex stainless steel. J Mater Process Technol 180:318–322. https://doi.org/10.1016/j.jmatprotec.2006.07.008
3. Bassani P, Breda M, Brunelli K, Mészáros I, Passaretti F, Zanellato M, Calliari I (2013) Characterization of a cold-rolled 2101 lean duplex stainless steel. Microsc Microanal 19:988–995. https://doi.org/10.1017/S1431927613001426
4. Li X, Lu K (2021) Refining grains of metals through plastic deformation: toward grain size limits. Accounts Mater Res 2:108–113. https://doi.org/10.1021/accountsmr.0c00075
5. Lowe TC, Valiev RZ (2004) The use of severe plastic deformation techniques in grain refinement. JOM 56:64–68. https://doi.org/10.1007/s11837-004-0295-z
6. Odnobokova M, Belyakov A, Kaibyshev R (2019) Grain refinement and strengthening of austenitic stainless steels during large strain cold rolling. Philos Mag 99:531–556. https://doi.org/10.1080/14786435.2018.1546961
7. Dixit US (2020) 1 - Modeling of metal forming: a review. In: Silberschmidt VV (ed) Mechanics of Materials in Modern Manufacturing Methods and Processing Techniques. Elsevier, pp 1–30. https://doi.org/10.1016/B978-0-12-818232-1.00001-1
8. Fargas G, Akdut N, Anglada M, Mateo A (2011) Reduction of anisotropy in cold-rolled duplex stainless steel sheets by using sigma phase transformation. Metall Mater Trans A 42:3472–3483. https://doi.org/10.1007/s11661-011-0744-6
9. Hamada J, Inoue H (2010) Texture and planar anisotropy of r-value in duplex stainless steel Sheet. Mater Trans 51:644–651. https://doi.org/10.2320/matertrans.MG200908
10. Grill A, Horky J, Panigrahi A, Krexner G, Zehetbauer M (2015) Long-term hydrogen storage in Mg and ZK60 after severe plastic deformation. Int J Hydrogen Energy 40:17144–17152. https://doi.org/10.1016/j.ijhydene.2015.05.145
11. Schwarz KT, Kormout KS, Pippan R, Hohenwarter A (2017) Impact of severe plastic deformation on microstructure and fracture toughness evolution of a duplex-steel. Mater Sci Eng A 703:173–179. https://doi.org/10.1016/j.msea.2017.07.062
12. Gamin YV, Muñoz Bolaños JA, Aleschenko AS, Komissarov AA, Bunits NS, Nikolaev DA, Fomin AV, Cheverikin VV (2021) Influence of the radial-shear rolling (RSR) process on the microstructure, electrical conductivity and mechanical properties of a Cu–Ni–Cr–Si alloy. Mater Sci Eng A 822:141676. https://doi.org/10.1016/j.msea.2021.141676
13. Valiev RZ, Islamgaliev RK, Alexandrov IV (2000) Bulk nanostructured materials from severe plastic deformation. Prog Mater Sci 45:103–189
14 Kapoor R (2017) Chapter 20 - severe plastic deformation of materials. In: Tyagi AK, Banerjee S (eds) Materials Under Extreme Conditions. Elsevier, Amsterdam, pp 717–754. https://doi.org/10.1016/B978-0-12-801300-7.00020-6
15. Muñoz JA, Nicoletti E, Signorelli JW, Stout MG, Avalos M, Bolmaro RE (2022) Effect of microstructural heterogeneity on the balanced-biaxial and tensile behavior of a Zn alloy sheet. Mater Today Commun 30:103126. https://doi.org/10.1016/j.mtcomm.2022.103126
16. Suwas S, Mondal S (2019) Texture evolution in severe plastic deformation processes. Mater Trans 60:1457–1471. https://doi.org/10.2320/matertrans.MF201933
17. Azushima A, Kopp R, Korhonen A, Yang DY, Micari F, Lahoti GD, Groche P, Yanagimoto J, Tsuji N, Rosochowski A, Yanagida A (2008) Severe plastic deformation (SPD) processes for metals. CIRP Ann 57:716–735. https://doi.org/10.1016/j.cirp.2008.09.005
18. Abid N, Khan AM, Shujait S, Chaudhary K, Ikram M, Imran M, Haider J, Khan M, Khan Q, Maqbool M (2022) Synthesis of nanomaterials using various top-down and bottom-up approaches, influencing factors, advantages, and disadvantages: a review. Adv Colloid Interface Sci 300:102597. https://doi.org/10.1016/j.cis.2021.102597
19. Wang L, Benito JA, Calvo J, Cabrera JM (2017) Twin-induced plasticity of an ECAP-processed TWIP steel. J Mater Eng Perform 26:554–562. https://doi.org/10.1007/s11665-016-2400-1
20. Zherebtsov S, Salishchev G, Galeyev R, Maekawa K (2005) Mechanical properties of Ti6Al4V titanium alloy with submicrocrystalline structure produced by severe plastic deformation.

Mater Trans 46:2020–2025. https://doi.org/10.2320/matertrans.46.2020
21. Khelfa T, Muñoz-Bolaños JA, Li F, Cabrera-Marrero JM, Khitouni M (2019) Microstructure and mechanical properties of AA6082-T6 by ECAP under warm processing. Met Mater Int. https://doi.org/10.1007/s12540-019-00388-y
22. Muñoz JA, Khelfa T, Komissarov A, Cabrera J-M (2020) Ductility and plasticity of ferritic-pearlitic steel after severe plastic deformation. Mater Sci Eng A 805:140624. https://doi.org/10.1016/j.msea.2020.140624
23. Muñoz JA, Higuera OF, Cabrera JM (2017) Microstructural and mechanical study in the plastic zone of ARMCO iron processed by ECAP. Mater Sci Eng A 697:24–36. https://doi.org/10.1016/j.msea.2017.04.108
24. Muñoz JA, Cobos OFH, M'Doihoma R, Avalos M, Bolmaro RE (2019) Inducing heterogeneity in an austenitic stainless steel by equal channel angular sheet extrusion (ECASE). J Mater Res Technol 8:2473–2479. https://doi.org/10.1016/j.jmrt.2019.04.013
25. Nilsson J-O (1992) Super duplex stainless steels. Mater Sci Technol 8:685–700. https://doi.org/10.1179/mst.1992.8.8.685
26. Francis R, Byrne G (2021) Duplex stainless steels—alloys for the 21st century. Metals (Basel) 11. https://doi.org/10.3390/met11050836
27. Chen TH, Weng KL, Yang JR (2002) The effect of high-temperature exposure on the microstructural stability and toughness property in a 2205 duplex stainless steel. Mater Sci Eng A 338:259–270. https://doi.org/10.1016/S0921-5093(02)00093-X
28. Gutiérrez-Vargas G, Ruiz A, Kim J-Y, López-Morelos VH, Ambriz RR (2019) Evaluation of thermal embrittlement in 2507 super duplex stainless steel using thermoelectric power. Nucl Eng Technol 51:1816–1821. https://doi.org/10.1016/j.net.2019.05.017
29. Santos RM, Rodrigues DG, Dias Santos ML, Santos DB (2022) Martensite reversion and strain hardening of a 2304 lean duplex stainless steel subjected to cold rolling and isochronous annealing at low temperatures. J Mater Res Technol 16:168–186. https://doi.org/10.1016/j.jmrt.2021.11.122
30. Biserova-Tahchieva A, Chatterjee D, van Helvoort ATJ, Llorca-Isern N, Cabrera JM (2022) Effect of the nanostructuring by high-pressure torsion process on the secondary phase precipitation in UNS S32750 Superduplex stainless steel. Mater Charact 183:111639. https://doi.org/10.1016/j.matchar.2021.111639
31. Llorca-Isern N, López-Luque H, López-Jiménez I, Biezma MV (2016) Identification of sigma and chi phases in duplex stainless steels. Mater Charact 112:20–29. https://doi.org/10.1016/j.matchar.2015.12.004
32. Tao P, Gong J, Wang Y, Jiang Y, Li Y, Cen W (2018) Characterization on stress-strain behavior of ferrite and austenite in a 2205 duplex stainless steel based on nanoindentation and finite element method. Results Phys 11:377–384. https://doi.org/10.1016/j.rinp.2018.06.023
33. Besharatloo H, Carpio M, Cabrera J-M, Mateo AM, Fargas G, Wheeler JM, Roa JJ, Llanes L (2020) Novel mechanical characterization of austenite and ferrite phases within duplex stainless steel. Metals (Basel) 10. https://doi.org/10.3390/met10101352.
34. Cao Y, Wang YB, An XH, Liao XZ, Kawasaki M, Ringer SP, Langdon TG, Zhu YT (2014) Concurrent microstructural evolution of ferrite and austenite in a duplex stainless steel processed by high-pressure torsion. Acta Mater 63:16–29. https://doi.org/10.1016/j.actamat.2013.09.030
35. Signorelli JW, Turner PA, Sordi V, Ferrante M, Vieira EA, Bolmaro RE (2006) Computational modeling of texture and microstructure evolution in Al alloys deformed by ECAE. Scr Mater 55:1099–1102. https://doi.org/10.1016/j.scriptamat.2006.08.042
36. Farias FA, Pontes MJH, Cintho OM (2010) Processing of a duplex stainless steel by equal channel angular extrusion. Matéria (Rio Janeiro) 15:345–354
37. Ajith PM, Sathiya P, Gudimetla K, Ravishankar B (2013) Mechanical, metallurgical characteristics and corrosion properties of equal channel angular pressing of duplex stainless steel. In: Key Eng. Mater. Comput. Sci. II, Trans Tech Publications Ltd, pp 9–14. https://doi.org/10.4028/www.scientific.net/AMR.717.9
38. Papavinasam S (2014) Chapter 6 - modeling – internal corrosion. In: Papavinasam S (ed) Corrosion Control in the Oil and Gas Industry. Gulf Professional Publishing, Boston, pp 301–360. https://doi.org/10.1016/B978-0-12-397022-0.00006-6
39. Iwahashi Y, Wang J, Horita Z, Nemoto M, Langdon TG (1996) Principle of equal-channel angular pressing for the processing of ultra-fine grained materials. Scr Mater 35:143–146. https://doi.org/10.1016/1359-6462(96)00107-8
40. Segal VM (1995) Materials processing by simple shear. Mater Sci Eng A 197:157–164. https://doi.org/10.1016/0921-5093(95)09705-8
41. Muñoz JA (2019) Geometrically Necessary Dislocations (GNDs) in iron processed by equal channel angular pressing (ECAP). Mater Lett 238:42–45. https://doi.org/10.1016/j.matlet.2018.11.142
42. Pantleon W (2008) Resolving the geometrically necessary dislocation content by conventional electron backscattering diffraction. Scr Mater 58:994–997. https://doi.org/10.1016/j.scriptamat.2008.01.050
43 Lebensohn RA, Castañeda PP, Brenner R, Castelnau O (2011) Full-field vs. homogenization methods to predict microstructure–property relations for polycrystalline materials. In: Ghosh S, Dimiduk D (eds) Computational Methods for Microstructure-Property Relationships. Springer US, Boston, pp 393–441. https://doi.org/10.1007/978-1-4419-0643-4_11
44 Tome C, Canova GR, Kocks UF, Christodoulou N, Jonas JJ (1984) The relation between macroscopic and microscopic strain hardening in F.C.C. polycrystals. Acta Metall 32:1637–1653. https://doi.org/10.1016/0001-6160(84)90222-0
45. Anglin BS, Gockel BT, Rollett AD (2016) Developing constitutive model parameters via a multi-scale approach. Integr Mater Manuf Innov 5:212–231. https://doi.org/10.1186/s40192-016-0053-4
46. Schwindt CD (2015) Desarrollo experimental y modelado computacional multiescala de la curva límite de formabilidad: aplicación a un acero dual-phase de alta resistencia, Universidad Nacional del Sur, Bahía Blanca. https://repositoriodigital.uns.edu.ar/handle/123456789/2532
47. Semiatin SL, DeLo DP (2000) Equal channel angular extrusion of difficult-to-work alloys. Mater Des 21:311–322. https://doi.org/10.1016/S0261-3069(99)00085-0
48. Bagherpour E, Reihanian M, Ebrahimi R (2012) On the capability of severe plastic deformation of twining induced plasticity (TWIP) steel. Mater Des 36:391–395. https://doi.org/10.1016/j.matdes.2011.11.055
49. Sun JL, Trimby PW, Yan FK, Liao XZ, Tao NR, Wang JT (2014) Shear banding in commercial pure titanium deformed by dynamic compression. Acta Mater 79:47–58. https://doi.org/10.1016/j.actamat.2014.07.011
50. Muñoz JA, Avalos M, Schell N, Brokmeier HG, Bolmaro RE (2021) Comparison of a low carbon steel processed by Cold Rolling (CR) and Asymmetrical Rolling (ASR): Heterogeneity in strain path, texture, microstructure and mechanical properties. J Manuf Process 64:557–575. https://doi.org/10.1016/j.jmapro.2021.02.017
51. Abib K, Balanos JAM, Alili B, Bradai D (2016) On the microstructure and texture of Cu-Cr-Zr alloy after severe plastic deformation by ECAP. Mater Charact 112:252–258. https://doi.org/10.1016/j.matchar.2015.12.026
52. Muñoz JA, Komissarov A, Avalos M, Bolmaro RE (2020) Mechanical and microstructural behavior of a heterogeneous austenitic stainless steel processed by Equal Channel Angular Sheet

Extrusion (ECASE). Mater Sci Eng A 792:139779. https://doi.org/10.1016/j.msea.2020.139779
53. Muñoz JA, Bolmaro RE, Jorge AM, Zhilyaev A, Cabrera JM (2020) Prediction of generation of high- and low-angle grain boundaries (HAGB and LAGB) during severe plastic deformation. Metall Mater Trans A 51:4674–4684. https://doi.org/10.1007/s11661-020-05873-3
54. Muñoz JA, Higuera OF, Tartalini V, Risso P, Avalos M, Bolmaro RE (2019) Equal channel angular sheet extrusion (ECASE) as a precursor of heterogeneity in an AA6063-T6 alloy. Int J Adv Manuf Technol 102:3459–3471. https://doi.org/10.1007/s00170-019-03425-7
55. Khelfa T, Muñoz-Bolaños J-A, Li F, Cabrera-Marrero J-M, Khitouni M (2021) Strain-hardening behavior in an AA6060-T6 alloy processed by equal channel angular pressing. Adv Eng Mater 23:2000730. https://doi.org/10.1002/adem.202000730
56. Muñoz JA, Higuera OF, Benito JA, Bradai D, Khelfa T, Bolmaro RE, Jorge AM, Cabrera JM (2019) Analysis of the micro and substructural evolution during severe plastic deformation of ARMCO iron and consequences in mechanical properties. Mater Sci Eng A 740–741:108–120. https://doi.org/10.1016/j.msea.2018.10.100
57. Yasnikov IS, Vinogradov A, Estrin Y (2014) Revisiting the Considère criterion from the viewpoint of dislocation theory fundamentals. Scr Mater 76:37–40. https://doi.org/10.1016/j.scriptamat.2013.12.009
58. Gil Sevillano J (2020) Dynamic steady state by unlimited unidirectional plastic deformation of crystalline materials deforming by dislocation glide at low to moderate temperatures. Metals (Basel) 10. https://doi.org/10.3390/met10010066
59. Tóth LS, Estrin Y, Lapovok R, Gu C (2010) A model of grain fragmentation based on lattice curvature. Acta Mater 58:1782–1794. https://doi.org/10.1016/j.actamat.2009.11.020
60. Kundu A, Field DP (2020) Influence of microstructural heterogeneity and plastic strain on geometrically necessary dislocation structure evolution in single-phase and two-phase alloys. Mater Charact 170:110690. https://doi.org/10.1016/j.matchar.2020.110690
61. Muñoz JA, Melia M, Avalos M, Bolmaro RE (2021) Equal channel angular sheet extrusion (ECASE) produces twinning heterogeneity in commercially pure titanium. Mater Charact 181:111460. https://doi.org/10.1016/j.matchar.2021.111460
62 Humphreys FJ, Hatherly M (2004) Chapter 4 - the structure and energy of grain boundaries. In: Humphreys FJ, Hatherly M (eds) Recrystallization and Related Annealing Phenomena, 2nd edn. Elsevier, Oxford, pp 91–119. https://doi.org/10.1016/B978-008044164-1/50008-6
63. Hazra SS, Gazder AA, Pereloma EV (2009) Stored energy of a severely deformed interstitial free steel. Mater Sci Eng A 524:158–167. https://doi.org/10.1016/j.msea.2009.06.033
64. Muñoz JA, Komissarov A, Mejía I, Hernández-Belmontes H, Cabrera J-M (2021) Characterization of the gas tungsten arc welding (GTAW) joint of Armco iron nanostructured by Equal-Channel Angular Pressing (ECAP). J Mater Process Technol 288:116902. https://doi.org/10.1016/j.jmatprotec.2020.116902
65. Tsuji N, Kamikawa N, Li BL (2007) Grain size saturation during severe plastic deformation. In: THERMEC 2006, Trans Tech Publications Ltd, pp 2837–2842. https://doi.org/10.4028/www.scientific.net/MSF.539-543.2837
66. Renk O, Pippan R (2019) Saturation of grain refinement during severe plastic deformation of single phase materials: reconsiderations, current status and open questions. Mater Trans 60:1270–1282. https://doi.org/10.2320/matertrans.MF201918
67. Calcagnotto M, Ponge D, Demir E, Raabe D (2010) Orientation gradients and geometrically necessary dislocations in ultrafine grained dual-phase steels studied by 2D and 3D EBSD. Mater Sci Eng A 527:2738–2746. https://doi.org/10.1016/j.msea.2010.01.004
68. Hansen N (2004) Hall-Petch relation and boundary strengthening. Scr Mater 51:801–806. https://doi.org/10.1016/j.scriptamat.2004.06.002
69. Weertman JR (1993) Hall-Petch strengthening in nanocrystalline metals. Mater Sci Eng A 166:161–167. https://doi.org/10.1016/0921-5093(93)90319-A
70. Park HK, Ameyama K, Yoo J, Hwang H, Kim HS (2018) Additional hardening in harmonic structured materials by strain partitioning and back stress. Mater Res Lett 6:261–267. https://doi.org/10.1080/21663831.2018.1439115
71. Muñoz JA, Komissarov A (2020) Back stress and strength contributions evolution of a heterogeneous austenitic stainless steel obtained after one pass by equal channel angular sheet extrusion (ECASE). Int J Adv Manuf Technol 109:607–617. https://doi.org/10.1007/s00170-020-05630-1